The Influence of Realistic Reynolds Numbers on Slat Noise Simulations

David P. Lockard[*] and Meelan M. Choudhari[†]

NASA Langley Research Center, Hampton, VA 23681

The slat noise from the 30P/30N high-lift system has been computed using a computational fluid dynamics code in conjunction with a Ffowcs Williams-Hawkings solver. Varying the Reynolds number from 1.71 to 12.0 million based on the stowed chord resulted in slight changes in the radiated noise. Tonal features in the spectra were robust and evident for all Reynolds numbers and even when a spanwise flow was imposed. The general trends observed in near-field fluctuations were also similar for all the different Reynolds numbers. Experiments on simplified, subscale high-lift systems have exhibited noticeable dependencies on the Reynolds number and tripping, although primarily for tonal features rather than the broadband portion of the spectra. Either the 30P/30N model behaves differently, or the computational model is unable to capture these effects. Hence, the results underscore the need for more detailed measurements of the slat cove flow.

Nomenclature

a	speed of sound
b	span
c	stowed chord
Cp	coefficient of pressure
c_s	slat chord
f	frequency
M	Mach number, $|\mathbf{V}_o|/a_o$
OASPL	overall SPL
p	pressure
PSD	power spectral density
Re_c	Reynolds number, $|\mathbf{V}_o|c/\nu_o$
rms	root mean square
S	distance along trajectory of cove shear layer
SPL	sound pressure level
St	Strouhal number, f^*c_s/U_o
TKE	turbulence kinetic energy

u, v, w	Cartesian fluid velocity components
U, V, W	time-averaged velocity components
$|\mathbf{V}|$	magnitude of velocity vector
$|\mathbf{V}_{2D}|$	planar velocity mangitude
x, y, z	Cartesian coordinates

Greek:

β	yaw angle
ρ	fluid density
ν	kinematic viscosity

Superscript:

$'$	perturbation quantity (e.g. $\rho' = \rho - \rho_\infty$)
$*$	dimensional quantity

Subscript:

∞	dimensionless free-stream quantity
o	dimensional free-stream reference quantity

I. Introduction

The non-propulsive (or airframe) sources of aircraft noise include high-lift devices (e.g., the leading-edge slat and trailing-edge flaps) and the aircraft undercarriage. The ranking of these sources is configuration dependent; however, both model-scale tests[1–6] and flyover noise measurements[7] have identified the leading-edge slat as a prominent source of airframe noise during aircraft approach. The slat noise spectrum is typically broadband, but may include one or more narrower peaks associated with aerodynamic and/or aeroacoustic resonances. Previous measurements indicate that the broadband spectrum has a maximum near Strouhal numbers between 1 and 3 (where the Strouhal number $= f^*c_s/|\mathbf{V}_o|$ is based on the free-stream velocity $|\mathbf{V}_o|$ and slat chord c_s), and exhibits a peak in the directivity in the lower aft quadrant at the corresponding frequency.[8] The overall sound pressure level (OASPL) for slat noise sources has been noted to scale with $M^{4.5}$ by Dobrzynksi[8] and M^5 by Guo,[9, 10] where M denotes the free-stream or flight Mach number. Mendoza[6] found that the overall sound pressure level scaled with M^5, but with something between M^4 and M^5 in the range of mid to high frequencies. However, as discussed in Refs. 8 and 10, the physical mechanisms underlying the observed characteristics of slat noise have not been fully explained as yet.

An essential ingredient to developing physics-based predictions of airframe noise involves synergistic combinations of experiments and numerical simulations for subcomponents. Recent studies of this type have provided a number of

---

[*]Aerospace Technologist, Computational AeroSciences Branch, Mail Stop 128, Senior Member, AIAA

[†]Aerospace Technologist, Computational AeroSciences Branch, Mail Stop 128, Associate Fellow, AIAA

American Institute of Aeronautics and Astronautics

useful physical insights into the noise source mechanisms that are responsible for the dominant features of the measured slat- and flap-noise spectra. Specifically, the high-frequency spectral hump in the slat noise measurements at NASA[2,5] has been attributed to vortex shedding from a finite thickness slat trailing edge.[11,12] The broadband component of slat noise at lower frequencies has been linked with the interaction between unsteady vortical structures in the slat cove region and the adjacent features of the high-lift geometry (viz., the slat trailing edge and the gap region between the slat and the main element).[13–15] The two-dimensional (2-D) computations of this type helped clarify the cause-effect relationships between the near-field flow structures and the far-field noise; however, a further assessment of these computations[16] indicated excessively energetic vortical structures in comparison with the PIV measurements.[17] Three-dimensional (3-D) computations over a narrow portion of the model span[18] led to significant improvement in that regard, yielding a favorable comparison with the PIV measurements.[17] The importance of 3-D fluctuations in determining the unsteady dynamics within the cove region has also been confirmed via computations for other high-lift configurations and using alternative numerical algorithms.[19,20]

The near-field fluctuations within the slat cove have been investigated experimentally[17] using the 30P/30N model. The 30P/30N model tested in the Basic Aerodynamic Research Tunnel (BART) at NASA Langley Research Center represents a generic, three-element, zero-sweep high-lift configuration with slat and flap deflections of 30 degrees each. The slat chord and flap chord of the model are equal to 15% and 30%, respectively, of the stowed chord of 18 in (0.457 m). For the approach configuration, the slat gap is 2.95%; the flap gap is 1.27%; and the slat and flap overhang settings are equal to -2.95% and 0.25% of the stowed chord, respectively. Reference 21 provides a definition of these rigging parameters. At the test Mach number of M = 0.17, the Reynolds number, Re_c, based on the stowed chord of the BART model, corresponds to 1.71 million. While this Reynolds number is substantially lower in comparison with full-scale applications, the BART experiment is still suitable for validating numerical predictions of the slat cove noise sources as described in Ref. 18. The BART measurements[17] consist of steady surface pressure measurements and extensive 2-D particle image velocimetry (PIV) data within the mid-span plane of the model.

The effect of the spanwise extent of the computational domain was investigated by Lockard and Choudhari[22] by increasing the span from 1" (37.3% of the slat chord as used in Ref. 18) to 6" (226% of the slat chord or 15% of the model span) while maintaining the same spanwise resolution. The simulations with the longer span indicated that the spanwise surface pressure correlations do not become smaller than 0.05 until around 2" (74.6% of the slat chord). The longer span also enabled predictions of the far-field noise without excessive assumptions about the near-field spanwise behavior. However, the spanwise correlation length of the acoustic signals was found to be on the order of a slat chord, so a much longer span than even 226% c_s would be needed to adequately propagate noise to the far-field at frequencies near the peak in the broadband signal. Nonetheless, the near-field unsteadiness that gives rise to the noise can be adequately modeled with a 2" span, allowing the shorter span to be used in parametric studies examining the source mechanism.

Although the slat geometry is basically 2-D, most modern aircraft have swept wings which will produce a spanwise flow. Imamura et al.[23] performed simulations of both swept and unswept wing configurations, but their results for the near-field unsteadiness were inconclusive as to the effect of the cross flow because the observed differences were deemed to be within their uncertainty. Dierke et al.[24] calculated the noise from the 30P/30N using a steady RANS solution to provide input to a stochastic turbulence method that calculated an acoustic source for a computational aeroacoustics simulation. Their 3-D simulations without sweep were able to reasonably approximate earlier 2-D computations by Bauer and Ewert[25] and also showed reasonable agreement with the simulations of Lockard and Choudhari.[22] Their cases with sweep exhibited similar spectral shapes to unswept cases, but tonal features were somewhat diminished. Lockard and Choudhari[26] also simulated the 30P/30N with two different freestream flows that included an imposed spanwise velocity to examine the effects of sweep. Their results indicated that the fluctuations and noise scaled primarily with the velocity normal to the leading edge rather than the total velocity. Furthermore, with this scaling, the spectral shape was relatively unchanged when sweep was imposed. They did observe different behavior in the tonal features between two cases with a spanwise flow. A case with a lower streamwise velocity and lower Reynolds number did not exhibit as pronounced tonal features. However, their simulations varied both the Mach and Reynolds numbers simultaneously in an attempt to keep the same boundary layer characteristics in the cross flow cases. Hence, the independent effects of the Mach number, Reynolds number, and cross flow could not be determined. In a subsequent paper, Lockard and Choudhari[27] examined the independent effects of Mach numbers in the range 0.13 to 0.25 and Reynolds numbers between 1.209 and 2.418 million. They found that the noise scaled approximately with the 5th power of the velocity, but had almost no dependence on the Reynolds number. In all of these cases, the tonal features were evident.

The influence of the angle of attack was examined by Choudhari et al.[28] The angle of attack was varied from 3.0° to 8.0°, with the broadband noise decreasing along with a corresponding rotation of the directivity pattern as the angle of attack increased. However, the general character of both the near-field unsteadiness within the slat cove region and the far-field acoustics were found to remain unchanged with the variation in the angle of attack. Furthermore, the tonal behavior was observed at all angles of attack.

American Institute of Aeronautics and Astronautics

The current effort seeks to computationally examine the effect of realistic Reynolds numbers on the noise radiated from the 30P/30N configuration. Numerous experiments[29–31] have observed tonal features in slat spectra from small-scale models at low Reynolds numbers, and some have had success reducing or eliminating them using tripping. The tonal features observed in 30P/30N simulations have been robust for the modest range of Reynolds numbers investigated previously. However, there is some experimental evidence that higher Reynolds may be required to see an effect. In experiments[5] conducted in the Low Turbulence Pressure Tunnel at NASA Langley, the noise from the Energy Efficient Transport (EET) 3-element high-lift system was examined for Reynolds numbers from 3.6 to 19 million. The noise was found to be relatively insensitive to Reynolds number variations above 7.2 million, although almost all of the differences in the slat spectra at Re_c 3.6 million were restricted to a high-frequency spectral hump attributed to trailing-edge shedding.[11,12] The tonal features under investigation in the current 30P/30N simulations occur at much lower frequencies, so the Re_c dependencies observed in the EET experiments may not be applicable to the 30P/30N slat case. However, the tripping that has been employed in experiments has had an effect on the lower frequency tones. The trips are typically used to enhance the transition to turbulence that would be experienced at higher Reynolds numbers. Therefore, it is important to determine the dependence of the noise over a range of Reynolds numbers that is more realistic than what has been examined previously.

The current simulations seek to examine the influence of the Reynolds number within the framework of simulations, and, hopefully, establish the relevance of low-Reynolds number slat aeroacoustic experiments. The first step is to determine if the computational model is sufficient to discern Reynolds number effects or if increased sophistication is required. If successful, isolating the independent effects of Re_c will be useful in guiding the development of simplified models for the noise and lay the foundation for future examinations of the effect of other significant parameters such as the angle of attack, slat deflection, slat gap, and noise reduction devices.

II.   Computational Simulations

The simulations use an extruded 2-D geometry (in the $x - y$ plane) with and without cross flow (in the z direction). Table 1 lists the parameters for the 5 cases under investigation. The velocities in the table and this paper are nondimensionalized by the free-stream speed of sound, and, therefore are equivalent to Mach numbers. For all but the last two of these cases, the freestream vertical and spanwise velocities are zero, so $|\mathbf{V}_\infty| = U_\infty$. In case 4, a $\beta = 35°$ sweep was simulated by imposing a spanwise flow of 0.12. For case 5, the total velocity is the same as in cases 1-3, but with $\beta = 45°$, the streamwise velocity is reduced to 0.12. Previous studies[26] have shown that the noise scales with the streamwise velocity and not the total velocity. The velocity normal to the leading edge is 0.17 in cases 1-4, and the Reynolds number is varied from 1.71 to 12.0 million.

As discussed in Ref. 26, sweep effects can be computationally modeled in different ways. The choice made here maintains the normal cross-section across the span and imposes a spanwise flow. Other possibilities could be more appropriate based on the actual physics of the problem, but the approach taken here is expected to at least capture the first-order effect of sweep.

Table 1. Case definitions.

	$|\mathbf{V}_\infty|$	U_∞	V_∞	W_∞	β	$\mathrm{Re}_c \times 10^6$
Case 1	0.17	0.17	0.0	0.0	0°	1.71
Case 2	0.17	0.17	0.0	0.0	0°	7.20
Case 3	0.17	0.17	0.0	0.0	0°	12.0
Case 4	0.208	0.17	0.0	0.120	35°	12.0
Case 5	0.17	0.120	0.0	0.120	45°	12.0

The computational procedure closely follows that used for the simulations in Refs. 18, 22, 26, and 27. Version 6 of the CFL3D[32] flow solver developed at NASA Langley Research Center is used to solve the 3-D, time-dependent, Navier-Stokes equations using a finite-volume formulation; the full viscous fluxes in all three grid coordinates are retained during the present simulations. A hybrid approach is used where the RANS equations are solved in regions where the grid is insufficient to resolve the unsteady turbulent eddies, such as in boundary layers around solid bodies, and an implicit large eddy simulation (LES) is performed in regions where the grid can resolve the eddy dynamics. The simulations used a third-order upwind scheme with flux-difference splitting, which has been shown to provide second order spatial accuracy in previous applications of CFL3D.[32] Based on the spanwise correlation results of Ref. 22, a spanwise extent of 2" (74.6% of the slat chord) is used in the simulations.

American Institute of Aeronautics and Astronautics
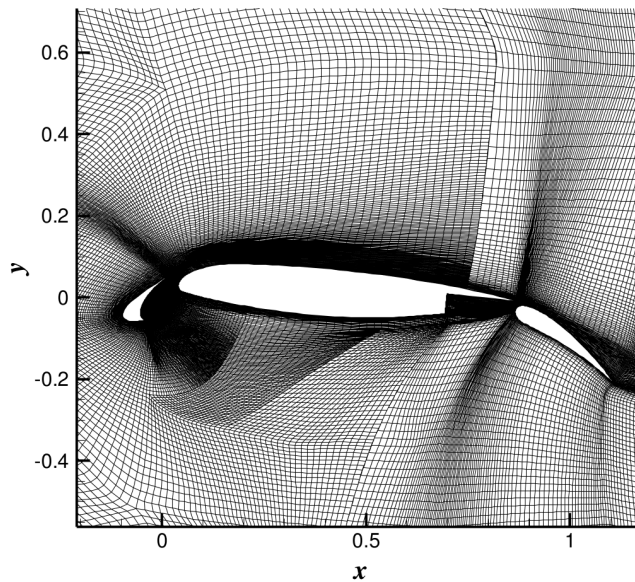
A. Configurations and Grids

Figure 1. Planar view of grid (every other point).

The 30P/30N[21] high-lift system was simulated in free air without any wind-tunnel walls. The trailing edge of each of the three elements has a finite thickness. However, following the approach taken in Ref. 22 for computational efficiency, all of the trailing edges (including the cusp or first edge of the slat) were artificially sharpened while preserving the camber of the respective sections. The investigated configuration corresponds to 4° angle of attack in BART,[17] which approximates the mean slat loading for a free-flight configuration at 5.5° angle of attack. The block structured, $x - y$ planar grid shown in Fig. 1 contains a total of 563,741 points in 77 blocks. Care was taken so that the first point off the solid surfaces was at $y^+ < 1$. To generate the 3-D grids, the planar mesh was replicated along the span over a distance of 0.746 slat chords using 129 points for a total grid point count of 62 million. Most of the block interfaces are point-matched with a one-to-one correspondence from each side. Patched interfaces, where the grid is coarsened going from one block to its neighbor, were also employed but were restricted to regions away from the slat. The planar grid and spanwise grid spacing are identical to that used in Ref. 22 and 26, and they are based on the grid resolution studies in Ref. 18. The grid was developed for a nominal Reynolds number of 1.71 million, but still provides good resolution with $y^+ < 1$ for a Re_c of 7.2 million. At a Re_c of 12 million, y^+ does exceed unity in some localized regions, but $y^+ < 2$ is still maintained throughout the surface of each airfoil element. The grid would need to be modified to account for the thinner boundary layers at Re_c much higher than 12 million.

Characteristic boundary conditions were used along the far-field boundaries in the $x - y$ plane, except for extrapolation from the interior at the downstream boundary. The circular outer boundary was located 12 airfoil chords from a point in the slat cove. Periodic boundary conditions were used across the spanwise boundaries of the computational domain. No attempt was made to resolve the end effects associated with the presence of tunnel side walls in the experiments. No-slip conditions were imposed at the solid surfaces, along with an adiabatic wall thermal boundary condition.

The two-equation Shear Stress Transport (SST) model of Menter[33] was used to capture the mean flow behavior of the unresolved scales of motion in regions away from the slat cove region, whereas the turbulence production terms in the turbulence transport equations were switched off within the cove region[18] to eliminate the excessive diffusive effects of the turbulence model on the resolved unsteady flow structures. The designation SST-QL[34] refers to the combination of the SST turbulence model and a quasi-laminar cove. Due to a lack of experimental transition data along the solid surfaces, as well as to maintain consistency with the previous simulations,[14–16] the flow within the Reynolds-Averaged Navier Stokes (RANS) regions was treated as fully turbulent, allowing the boundary layer transition locations along all three elements to be determined by the SST turbulence model. Previous computations have also been performed using a modified version of the Delayed Detached Eddy Simulation,[34] and no significant differences were observed with the quasi-laminar approach. Therefore, to maintain consistency with the majority of the previous calculations, the quasi-laminar approach with the SST model is used in this paper.

CFL3D employs a dual-time-stepping algorithm with subiterations used to converge the solution within each time step. Fifteen subiterations were used per time step to reduce the residual by a minimum of three orders of magnitude. The

time step was $dt^* a_o/c = 0.0016232$ or $dt^* |\mathbf{V_o}|/c = 0.00028$ which results in 453 time steps per period at a frequency of 1 kHz. The corresponding convective scale for a particle traveling with the flow to traverse the stowed chord of the airfoil is 3573 time steps. The time step used in the current simulations is larger than those used in some earlier studies of the 30P/30N configuration[16,18] because the trailing-edges have been sharpened to avoid any high-frequency vortex shedding behind the trailing edges. Based on the time-step study performed in Ref. 22, the step size used in the current simulations should be sufficient to resolve the broadband component of the slat fluctuations which is the focus of the present study.

The simulation procedure includes several steps. First, a steady-state computation was used to set up the basic mean flow, followed by an unsteady calculation with random suction and blowing applied to different spanwise and azimuthal sections of the slat in order to accelerate the onset of 3-D, unsteady flow structures. The forcing did not exceed 3% of the freestream velocity. The forcing was turned off after significant unsteadiness was observed, typically a few hundred time steps into the unsteady calculation. The simulation was then run for at least 30,000 time steps to allow the transient flow field to wash out before collecting time records. After this phase, well-resolved, unsteady structures develop in the slat cove region. There is also some unsteadiness associated with a separated region on the flap. The grid is too coarse to resolve the unsteady flow around the flap, and these fluctuations eventually settle down to levels that do not significantly impact the slat cove region. In the real flow, the oscillations in the flap separated region are probably persistent and much stronger, but the purpose of the current study is to isolate the slat cove dynamics. Therefore, the observed damping behavior in the flap region is actually intended and advantageous. Averaged flow quantities were produced by time-averaging over a minimum of 39,000 time steps. To increase the number of averages, a second averaging process was performed in the spanwise direction. Although shear layers can exhibit inhomogeneous spanwise behavior, assuming spanwise homogeneity of the flow statistics is consistent with the observations of this particular flowfield.

III.   Near-Field Results

The coefficient of pressure, $Cp = 2(p^* - p_o)/(\rho_o U_o^2)$, on the high-lift system is presented in Fig. 2. Note that the velocity normal to the leading edge is used in defining Cp rather than the total velocity. Previous studies[22] have shown that cases with a spanwise flow scale on U_o and not the total velocity. The results from the four calculations with different Reynolds numbers are included. The data was generated by averaging over time, then averaging over the span by assuming the flow is homogeneous in that direction. The slight jump on the pressure side at $x^*/c = 0.7$ is caused by the geometric discontinuity where the flap cove begins. The high Re_c data from Low-Turbulence Pressure Tunnel (LTPT) experiments of the 30P/30N from Ref. 35 (Fig. 12a) show a substantially reduced extent of flap separation between Re_c of 6 and 9 million which influences the loading on the slat. Similarly, the results for the two cases with $Re_c \geq 7.2$ million are nearly on top of each other and exhibit decreased flap separation and increased overall lift. The addition of the spanwise flow at $Re_c = 12.0$ million while maintaining the same streamwise velocity has a much smaller impact on the results. However, the case with the lower streamwise velocity shows even less flap separation. Nonetheless, the overall impact on the slat pressure distribution is minimal.

A comparison of the calculated Cp'_{rms} is shown in Fig. 3. The Cp'_{rms} reaches a maximum near the reattachment point in the slat cove at $x^*/c = 0.005$. The 5 curves do not collapse in that region, with the cases with spanwise flow exhibiting the highest fluctuation levels that are approximately 10% greater in comparison with the no-mean spanwise flow cases. The case with spanwise flow may not be scaling exactly with the characteristic velocity U_o, but the collapse using the total free-steam velocity $|V_o|$ is much worse. Overall, the discrepancies are really quite small when considering how much influence they would have on the radiated noise which is typically represented on a logarithmic scale.

The magnitude of the planar velocity $|\mathbf{V}_{2D}^*|$, nondimensionalized by U_o, is compared in Fig. 4. The velocity distributions are quite similar for all the computations. The same nominal trajectory of the shear layer, shown as the purple line, is superimposed in all the figures. However, the stagnation points and shear layer trajectories are moved slightly upstream in all the higher Re_c cases. Furthermore, the 3-D turbulence kinetic energy (TKE), $\frac{1}{2}(<u'u'> + <v'v'> + <w'w'>)$, normalized by the square of the streamwise velocity, U_o^2, reveals some differences as seen in Fig. 5. The thin region of high 3-D TKE near the reattachment point and extending to the trailing edge is more pronounced when the spanwise flow is added. The spanwise fluctuations are primarily responsible for the high TKE in this region. Just below this region is another, larger area of enhanced TKE where the vertical velocity fluctuations peak. The elevated TKE levels are caused by instabilities in the cove shear layer being rapidly distorted as they approach the underside of the slat.[18] In this region, the TKE decreases slightly as the Reynolds number is increased, and then more dramatically as the spanwise flow is added. Some other differences between the four cases are evident such as the region of low TKE in the cove (indicated by the blue regions) being more pronounced at the lowest Reynolds number.

The power spectral density (PSD) of the surface pressure at the 6 points identified in Fig. 4 are presented in Fig. 6.
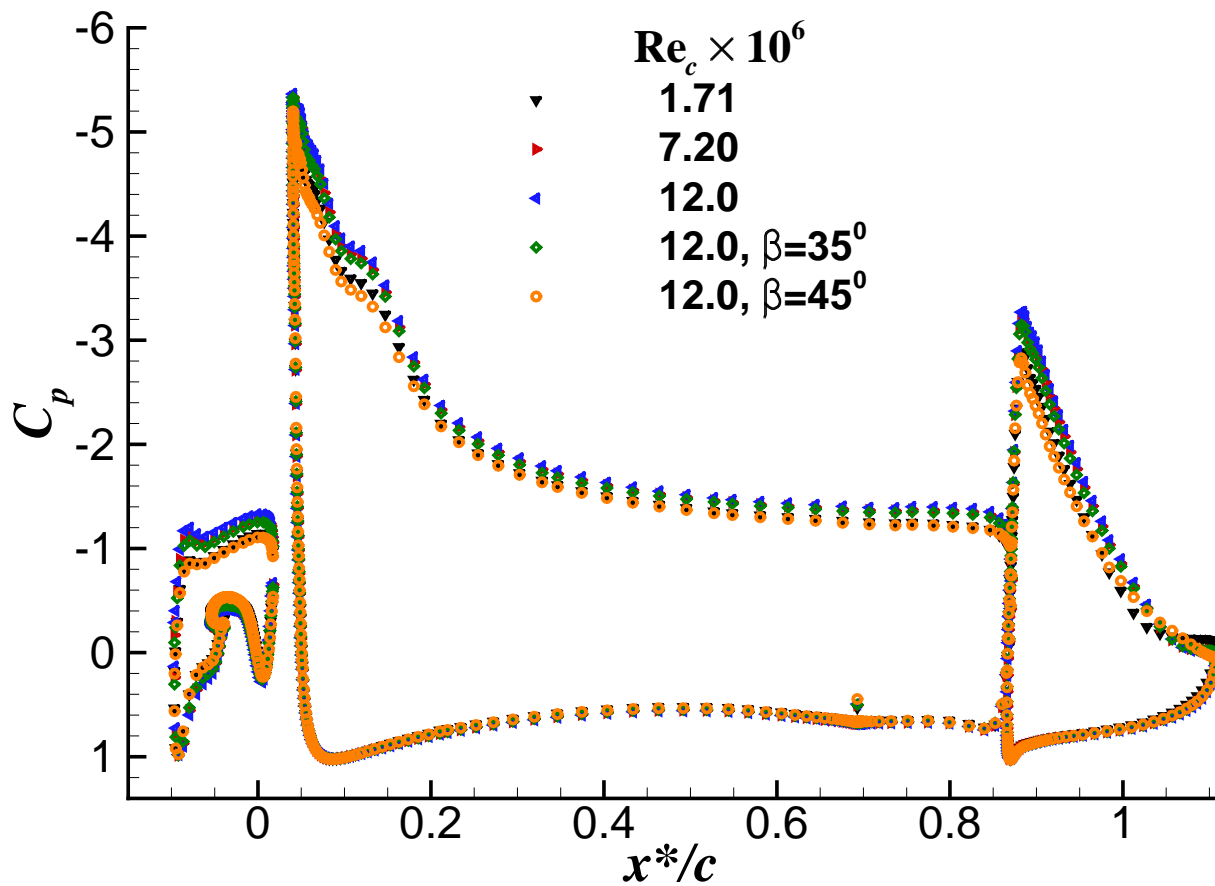
American Institute of Aeronautics and Astronautics
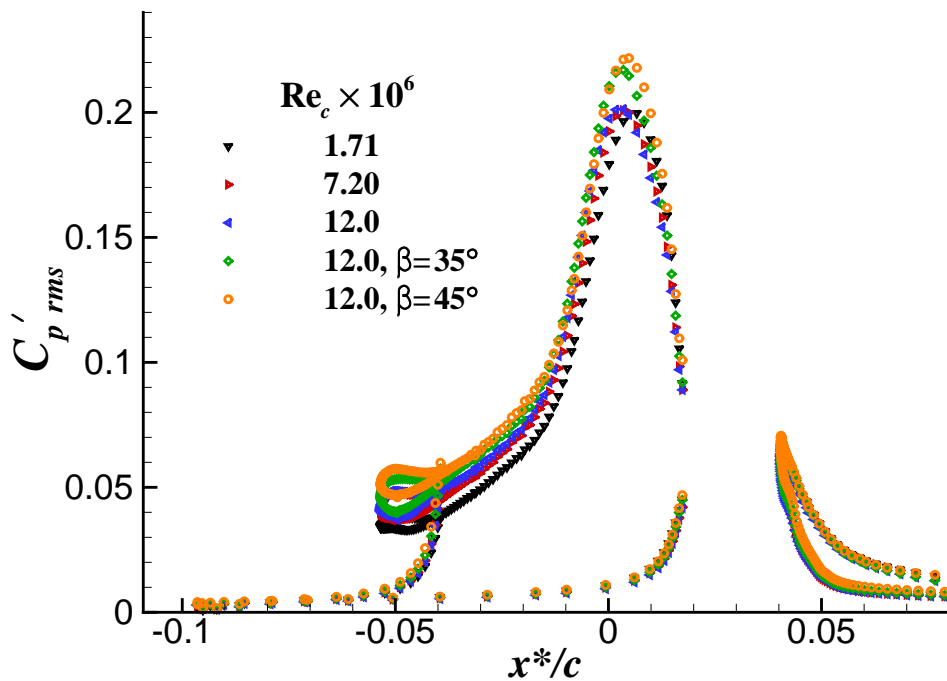
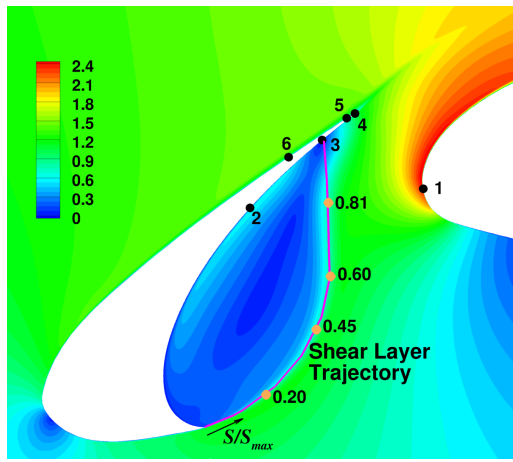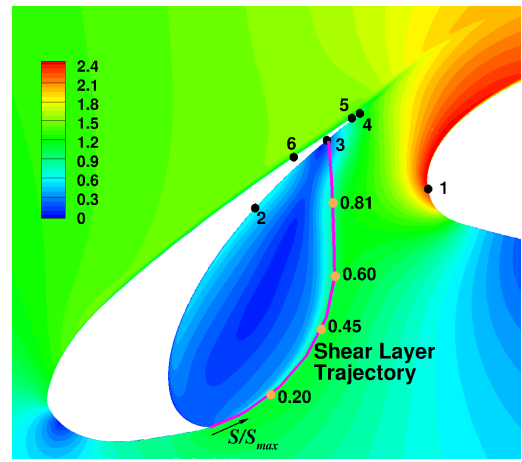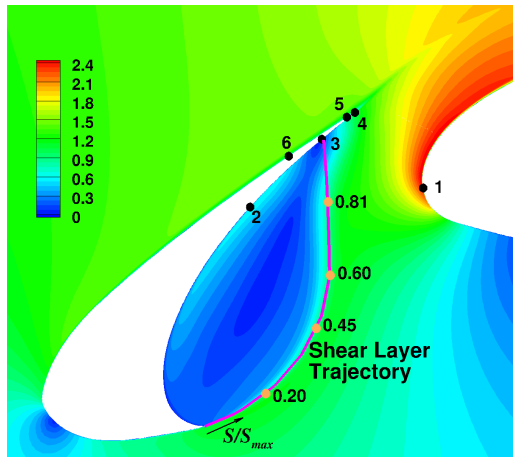**Figure 2. Coefficient of pressure on the airfoil.**

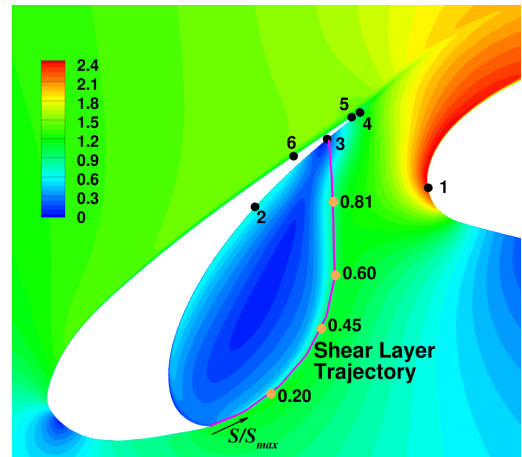**Figure 3. RMS of the coefficient of pressure on the airfoil.**
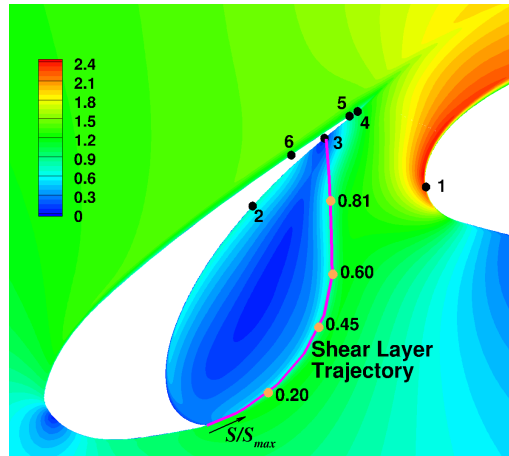
(a) $Re_c = 1.71 \times 10^6$

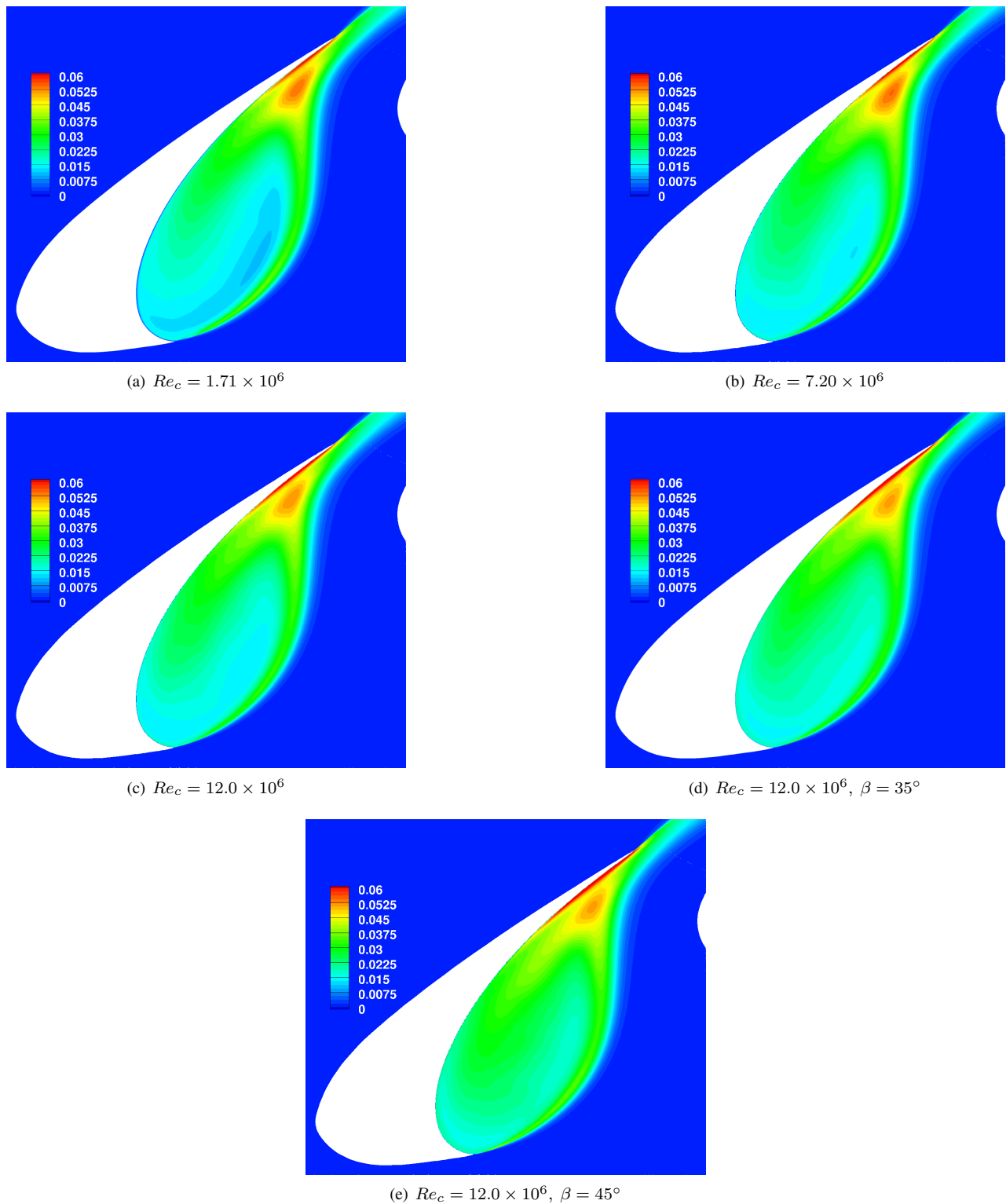(b) $Re_c = 7.20 \times 10^6$

(c) $Re_c = 12.0 \times 10^6$

(d) $Re_c = 12.0 \times 10^6$, $\beta = 35°$

(e) $Re_c = 12.0 \times 10^6$, $\beta = 45°$

Figure 4. Magnitude of the planar velocity, $|\mathbf{V}^*_{2D}|/U_o$, around the slat averaged both temporally and in the spanwise direction. S is the distance along the shear layer trajectory, and S/S_{max}=0.21, 0.45, 0.60, 0.82 correspond to four points in the shear layer that will be examined. The surface pressure at the points numbered 1 to 6 will also be examined.

The amplitude has been adjusted assuming $p' \sim U_\infty^2$, with the reference streamwise velocity as 0.17, as this produced a reasonable collapse of the rms data. The power spectral density is plotted against the Strouhal number, $St = f^* c_s / U_o$, based on the streamwise velocity U_o, and the slat chord, c_s. Except for points 2, 3 and 4, the scaling does a good job of

American Institute of Aeronautics and Astronautics

(a) $Re_c = 1.71 \times 10^6$

(b) $Re_c = 7.20 \times 10^6$

(c) $Re_c = 12.0 \times 10^6$

(d) $Re_c = 12.0 \times 10^6$, $\beta = 35°$

(e) $Re_c = 12.0 \times 10^6$, $\beta = 45°$

Figure 5. 3-D Turbulence kinetic energy normalized by U_o^2 around the slat averaged both temporally and in the spanwise direction.

collapsing the data. Point 2 is within the recirculation region which experiences a high degree of intermittency, so the uncertainty in the statistics is likely to be high. Hence, disagreement there is not unexpected. At points 3 and 4, only the cases with a spanwise flow are different from the others. However, for points 1, 5, and 6, all of the cases exhibit very similar behavior. These points should be most representative of the radiated noise as they are not as influenced by the hydrodynamic fluctuations in the cove. The $\beta = 45°$ case does not agree as well with the others, but it is the only case

with a different U_o (see Table 1). The U_o is used in both the amplitude and frequency scaling. For the two points 5 and 6 on the upper surface of the slat, the signals exhibit distinct peaks. When such peaks are found in experiments, tripping the boundary layer on the under-surface of the slat or running at higher Reynolds numbers often eliminates these tonal features. However, they are still quite evident in the simulations at $Re_c = 12$ million, with and without a spanwise flow. Furthermore, these peaks collapse reasonably well based on St.

The PSDs of the velocities in the cove region at the 4 points identified along the shear layer trajectory in Fig. 4 are presented in Figs. 7 and 8. As indicated in the label of the ordinate in the figures, the PSDs of the case with a different streamwise velocity have been scaled by $(U_{ref}/U_\infty)^2$, where $U_{ref} = 0.17$, the value of U_∞ for Cases 1 to 4. This assumes that the velocity fluctuations are scaling with the 2nd power of the mean streamwise velocity. Although Re_c and U_∞ influence the results near the cusp ($S/S_{max} = 0.2$), the differences diminish along the shear layer trajectory until the discrepancies are relatively small near the reattachment point ($S/S_{max} = 0.81$). The spectra along the trajectory should be representing the convective history of instabilities growing in the shear layer. Interestingly, the variation in the early development has little influence on the later fluctuations. Also, the spanwise flow has a greater impact on the spectra than Re_c. The two cases with a spanwise flow even exhibit somewhat pronounced peaks between St of 1 and 2 for $S/S_{max} \leq 0.6$. The tones in both the u and v spectra do not scale with St, but appear at the same frequency for the two cases. However, the tones do not appear to have any lasting influence and may not be important.
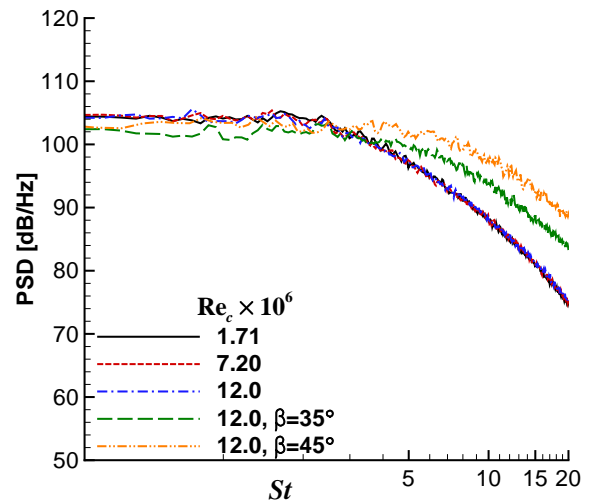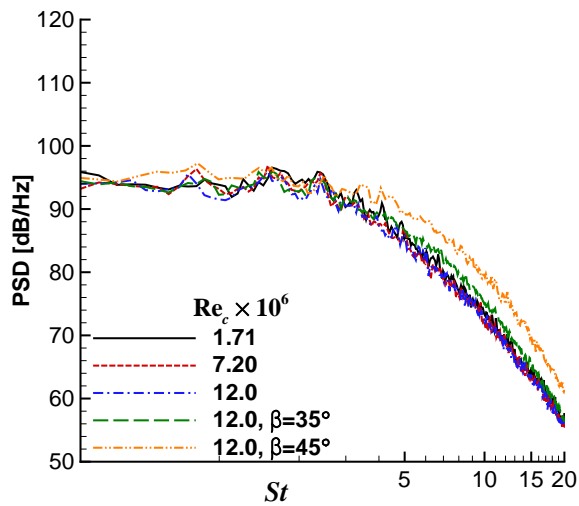
American Institute of Aeronautics and Astronautics
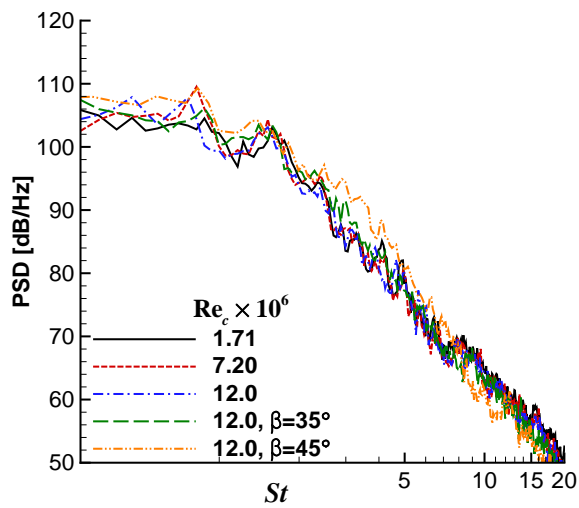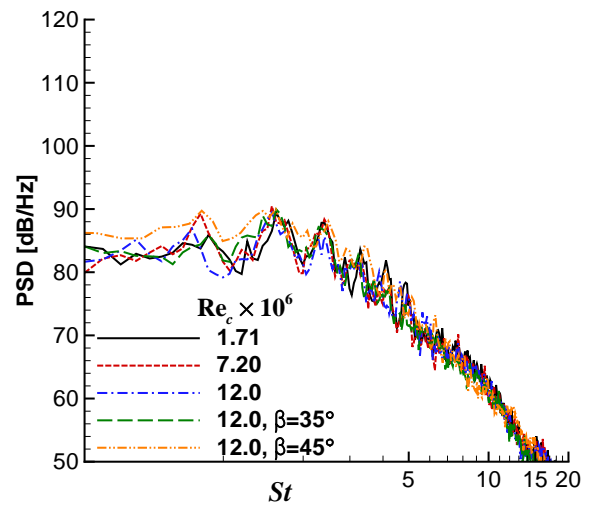
(a) Point 1
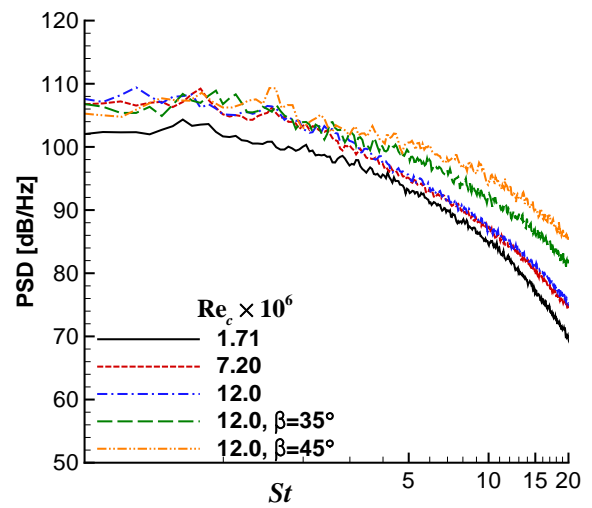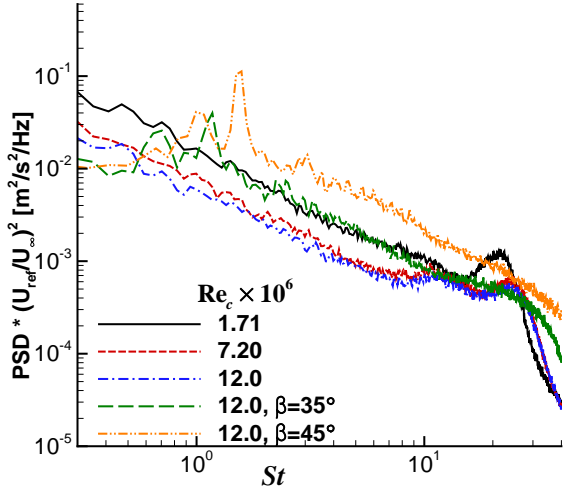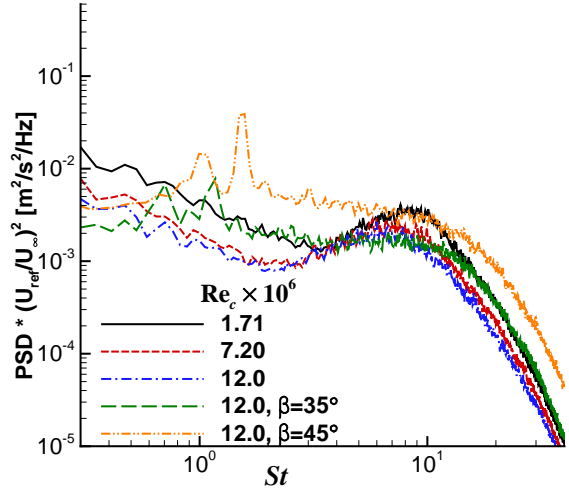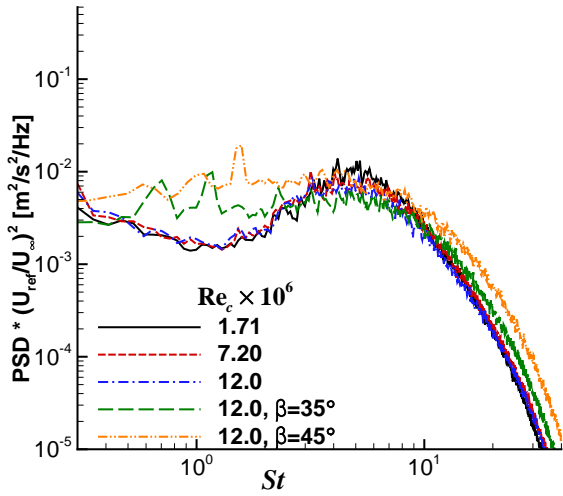
(b) Point 2
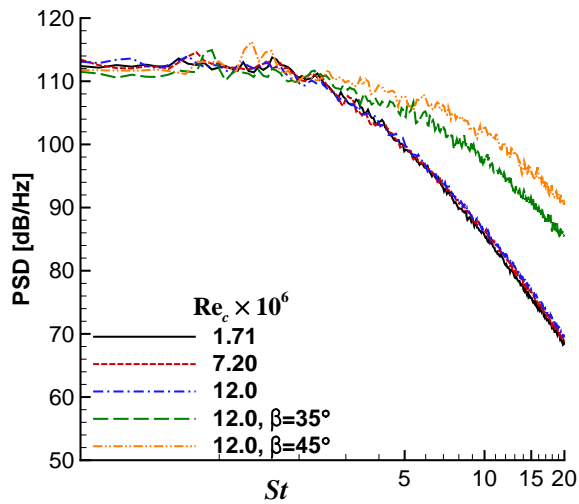
(c) Point 3

(d) Point 4

(e) Point 5

(f) Point 6

Figure 6. Power spectral density versus Strouhal number at the 6 points in Fig. 4. Data scaled assuming $p' \sim U_\infty^2$ **with 0.17 as the reference streamwise velocity.**
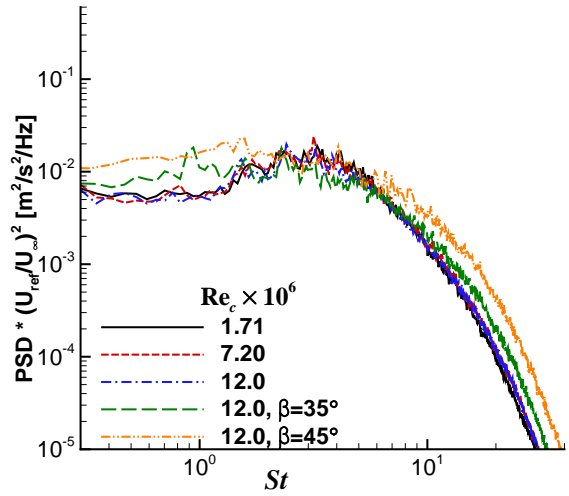
(a) S/S_{max}=0.20

(b) S/S_{max}=0.45

(c) S/S_{max}=0.60

(d) S/S_{max}=0.81

Figure 7. Power spectral density of the u velocities versus Strouhal number at 4 locations defined by S/S_{max} along the trajectory of the slat cove shear layer shown in Fig. 4. The scaling of the PSDs to account for different streamwise velocities uses the reference velocity $U_{\mathrm{ref}} = 0.17$.

American Institute of Aeronautics and Astronautics

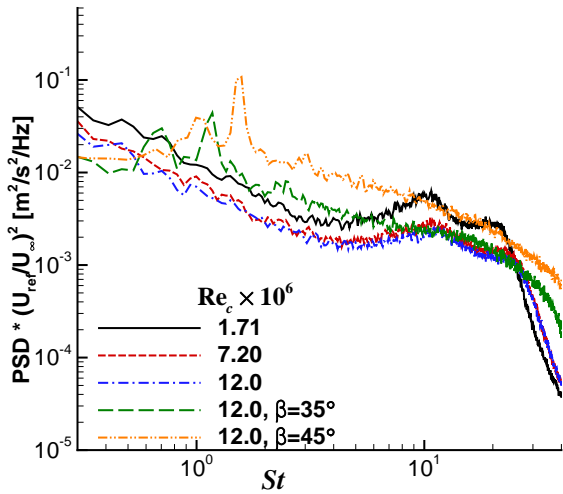(a) $S/S_{max}=0.20$

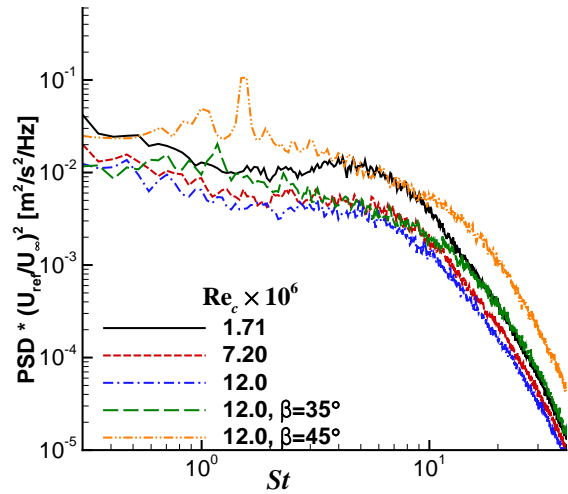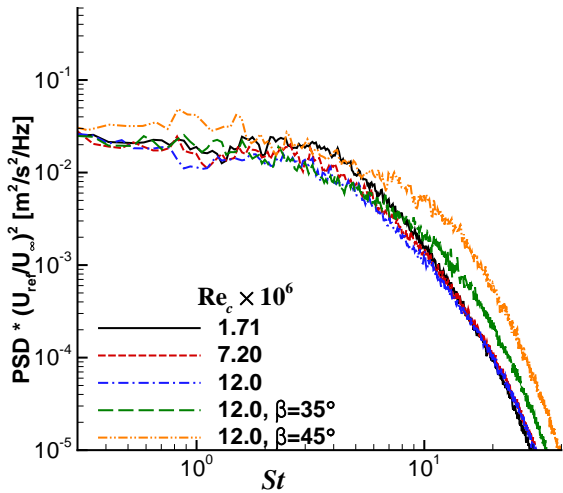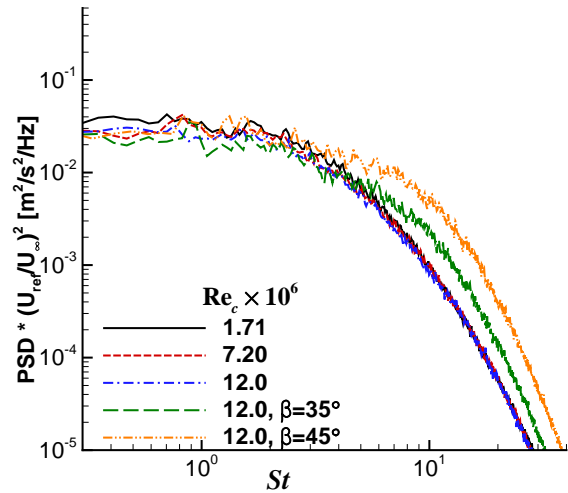(b) $S/S_{max}=0.45$

(c) $S/S_{max}=0.60$

(d) $S/S_{max}=0.81$

Figure 8. Power spectral density of the v velocities versus Strouhal number at 4 locations defined by S/S_{max} along the trajectory of the slat cove shear layer shown in Fig. 4. The scaling of the PSDs to account for different streamwise velocities uses the he reference velocity $U_{ref} = 0.17$.

American Institute of Aeronautics and Astronautics

A. Acoustics

The far-field noise was calculated using the Ffowcs Williams-Hawkings (FW-H) equation[36] frequency-domain solver described by Lockard.[37] Calculations were also performed with a time-domain[37] solver, and the directivity and spectral results were in agreement with those shown here from the frequency-domain solver. Unsteady flow data from the CFD calculations was recorded on the solid surfaces, with the data extracted over the full span used in the CFD calculation. However, only half of the spanwise data were used in the FW-H calculations to avoid artificial interference effects caused by the periodic nature of the simulations. Hence, the noise predictions are for a spanwise segment that is 37% of the slat chord (approximately 1 in or 2.54 cm). Predictions for longer spans could be calculated using corrections[38] for the actual span of a body. The temporal record of 39,000 time steps was divided into 7 separate segments, where successive segments were overlapped by 50%. Each segment was run through the FW-H solver independently, and the 7 individual results were then averaged.

The directivity is shown in Fig. 9. The distance from the slat trailing edge to the observers is 10 chords. The noise exhibits $1/r$ decay at this distance as demonstrated in Ref. 22. The directivity was calculated for Strouhal numbers between 0.3 and 20 so that very low- and very high-frequency oscillations that are not adequately represented within the near-field data are excluded. The length of each data segment is sufficient to resolve $St = 0.3$ with approximately 6 periods. As is evident in the figure, the higher Reynolds number cases do not exhibit all the lobes that are seen at $Re_c = 1.71 \times 10^6$, although the general pattern is quite similar. The magnitude does decrease slightly with increasing Reynolds number, although the inclusion of a spanwise flow with the same U_o produces a slight increase in the noise. The $\beta = 45°$ case with $U_o = 0.12$ was scaled assuming $p'^2 \sim U_o^5$. With such a scaling, this case exhibits less noise in the upstream direction but similar radiation below the wing. Nonetheless, all the differences would be very small on a decibel scale.
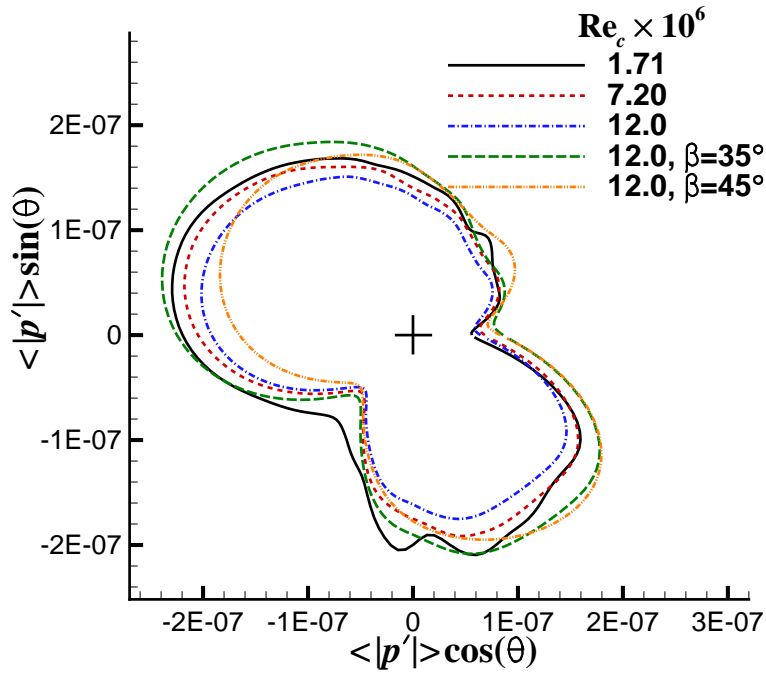

Figure 9. FW-H predictions of the directivity. Observers are 10 chords from the slat trailing edge. The $\beta = 45°$ case scaled with $p'^2 \sim U_o^5$.

The power spectral density of the pressure at four points between $270°$ and $330°$ (i.e., within the rear arc) are presented in Fig. 10. The current data represent the average of 7 realizations with a bin width of $\Delta St = 0.074$ at $U_\infty = 0.17$, corresponding to 48 Hz. Unfortunately, the simulation data record is not long enough to allow sufficient averaging to smooth the curves as much as desired without using an excessively large bin width. At $270°$ the peaks from the lowest Reynolds number case are a bit more prominent than for the other cases, but this may be a result of a slightly different directivity for the peaks and corresponds to where the extra lobes are evident in the directivity. Furthermore, the higher Re_c cases seem to have more tonal character than the lowest Reynolds number case for $St < 2$. At the other three angles, the curves for all the cases are similar, although again the lowest Reynolds number case shows slightly more prominent peaks for $St > 2$. The case with spanwise flow and $U_o = 0.17$ does exhibit marginally elevated levels above $St = 5$, but these levels are well below the peak in the spectrum. Again, the $\beta = 45°$, $U_o = 0.12$ case has been scaled

assuming $p'^2 \sim U_o^5$. At 310° and 330°, the $\beta = 45°$ case exhibits slightly higher levels than the others for $St > 2$. In addition, the two cases with a spanwise flow exhibit less tonal character, especially for $St < 2$. However, some tonal features are still evident in all the cases, and all the spectral shapes are qualitatively and even somewhat quantitatively similar. The tonal features appear to be robust with respect to changes in Re_c and the spanwise flow. The variations observed in previous experiments and computations are not evident in the present simulation results.
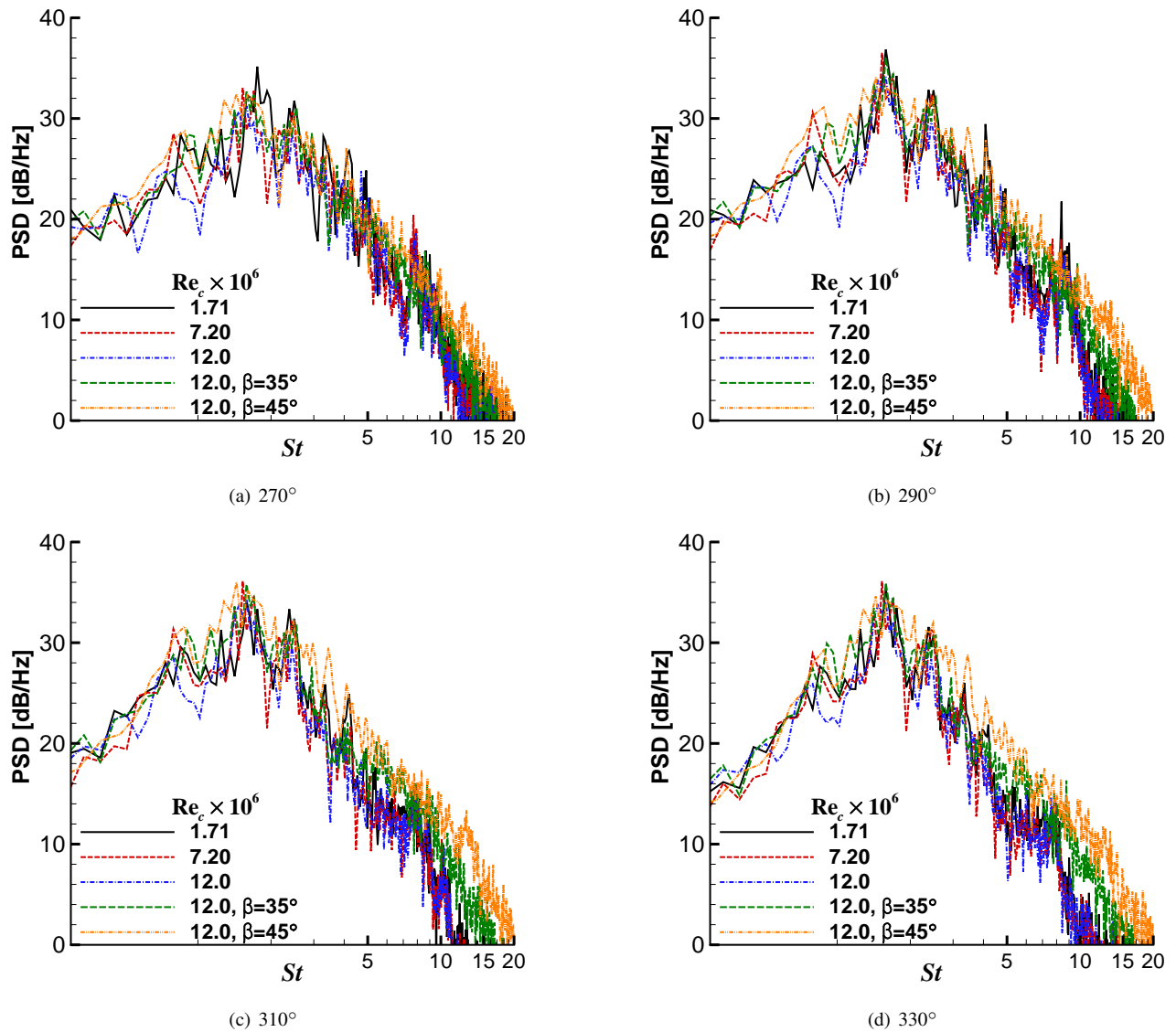

(a) 270°

(b) 290°

(c) 310°

(d) 330°

Figure 10. FW-H predictions of the power spectral density versus Strouhal number at several angles for observers located 10 chords from the slat trailing edge.

Conclusions

The present simulations help document the effect of Reynolds number on computed slat noise. Such an understanding is needed for a deeper assessment of simulation based predictions of slat noise and their applications to improved reduced-order models as well as to lay the foundation for simulation-based assessments of important parametric trends related to variations in the angle of attack, slat gap, and slat deflection.

The current simulations do not exhibit a strong dependence on Reynolds number between $1.71 \times 10^6 < Re_c < 12 \times 10^6$. This is true of both the broadband noise and tonal features in the spectra. The tonal features are somewhat stronger at the lowest Reynolds number, but the differences are on the order of the uncertainty in the results. The effect of the Reynolds number on the flow can be manifested in three ways. First, at low Re_c, the boundary layer can transition

American Institute of Aeronautics and Astronautics

upstream of the slat cusp, resulting in higher fluctuation levels in the separating shear layer. However, this scenario is unlikely for the range of Reynolds numbers studied because of the strong favorable pressure gradient and lack of surface roughness on the underside of the slat. Furthermore, because the calculations were run fully turbulent, the turbulence model will be prone to transition at geometric discontinuities, such as the slat cusp. Second, the spatial evolution of the separating shear layer should be affected by the Reynolds number. Although the simulations do indicate some minor changes, experimental data describing the evolution of the cove shear at different Reynolds numbers is not currently available to confirm what kind of changes should be expected. Third, thinner boundary layers associated with higher Re_c have a higher resistance to separation, so separation patterns are influenced thereby affecting the overall loading and stagnation points. Hence, the velocity at the cusp and the reattachment point in the cove are influenced by the Reynolds number. Although these effects are evident in the simulations and follow the trends observed in LTPT experiments,[35] their impact on the noise was found to be minimal in the simulations.

Geometric differences between the 30P/30N and other experimental wind-tunnel models may be responsible for the different observed Re_c dependencies of tonal features in the spectra, or the simulations, and in particular the turbulence model, may not be modeling the physics that is responsible for the low-Reynolds number acoustic behavior observed in the experiments. All of the cases here have been run in a quasi-laminar mode that does not include any transitional effects that may be present in experiments. Unsteadiness associated with a laminar separation bubble on the slat or the separated region of the flap could not be adequately resolved with the current method and grid. Although a grid resolution study has been performed for the current grid system[18] for the baseline $Re_c = 1.71 \times 10^6$, none of the grids studied may be fine enough to capture sufficiently the near wall dynamics or full details of transition in the slat cove shear layer. In particular, the spanwise resolution may be inadequate for the higher Reynolds number cases examined here. At all the Reynolds numbers examined computationally, the simulations exhibited tonal spectral features that are often attributed to transitional effects which should not be present in the high Reynolds number calculations. The exact cause of the tonal features remains unknown. Despite many previous computational and experimental studies of the 30P/30N configuration, the exact mechanism responsible for the tones, and even the broadband noise, has not been identified. Further coordinated studies with experiments and computations are needed to gain a better understanding of the slat noise generation process. Future experiments on the 30P/30N are planned that should be helpful in clarifying the dependence of slat noise on relevant parameters.

Acknowledgments

References

[1]Hayes, J. A., Horne, W. C., Soderman, P. T., and Bent, P. H., "Airframe Noise Characteristics of a 4.7% Scale DC-10 Model," AIAA Paper 1997-1594, 1997.

[2]Storms, B. L., Ross, J. C., Horne, W. C., Hayes, J. A., Dougherty, R. P., Underbrink, J. R., Scharpf, D. F., and Moriarty, P. J., "An Aeroacoustic Study of an Unswept Wing with a Three-Dimensional High Lift System," NASA TM 112222, February 1998.

[3]Dobrzynski, W., Nagakura, K., Gehlhar, B., and Buschbaum, A., "Airframe Noise Studies on Wings with Deployed High-Lift Devices," AIAA Paper 1998-2337, 1998.

[4]Storms, B. L., Hayes, J. A., Moriarty, P. J., and Ross, J. C., "Aeroacoustic Measurements of Slat Noise on a Three-Dimensional High-Lift System," AIAA Paper 1999-1957, 1999.

[5]Choudhari, M. M., Lockard, D. P., Macaraeg, M. G., Singer, B. A., Streett, C. L., Neubert, G. R., Stoker, R. W., Underbrink, J. R., Berkman, M. E., Khorrami, M. R., and Sadowski, S. S., "Aeroacoustic Experiments in the Langley Low-Turbulence Pressure Tunnel," NASA TM-211432, February 2002.

[6]Mendoza, F. and Brooks, T., "Aeroacoustic Measurements of a Wing/Slat Model," AIAA Paper 2002-2604, 2002.

[7]Chow, L. C., Mau, K., and Remy, H., "Landing Gears and High Lift Devices Airframe Noise Research," AIAA Paper 2002-2408, 2002.

[8]Dobrzynski, W. and Pott-Pollenske, M., "Slat Noise Source Studies for Farfield Noise Prediction," AIAA Paper 2001-2158, 2001.

[9]Guo, Y., Yamamoto, K., and Stoker, R., "Component Based Empirical Model for High-Lift System Noise Prediction," *Journal of Aircraft*, Vol. 40, No. 5, 2003, pp. 914–922.

[10]Guo, Y. and Joshi, M., "Noise Characteristics of Aircraft High-Lift Systems," *AIAA Journal*, Vol. 41, No. 7, 2003, pp. 1247–1256.

[11]Khorrami, M. R., Berkman, M. E., and Choudhari, M. M., "Unsteady Flow Compuations of a Slat with a Blunt Trailing Edge," *AIAA Journal*, Vol. 38, No. 11, 2000, pp. 2050–2058.

[12]Singer, B. A., Lockard, D. P., and Brentner, K. S., "Computational Aeroacoustic Analysis of Slat Trailing-Edge Flow," *AIAA Journal*, Vol. 38, No. 9, 2000, pp. 1558–1564.

[13]Khorrami, M. R., Singer, B. A., and Berkman, M. E., "Time-Accurate Simulations and Acoustic Analysis of Slat Free Shear Layer," *AIAA Journal*, Vol. 40, No. 7, 2002, pp. 1284–1291.

[14]Khorrami, M. R., Singer, B. A., and Lockard, D. P., "Time-Accurate Simulations and Acoustic Analysis of Slat Free Shear Layer: Part II," AIAA Paper 2002-2579, 2002.

[15]Choudhari, M. M., Khorrami, M. R., Lockard, D. P., Atkins, H. L., and Lilley, G. M., "Slat Cove Noise Modeling: A Posteriori Analysis of Unsteady RANS Simulations," AIAA Paper 2002-2468, 2002.

[16]Khorrami, M. R., Choudhari, M. M., and Jenkins, L. M., "Characterization of Unsteady Flow Structures Near Leading-Edge Slat: Part II. 2-D Computations," AIAA Paper 2004-2802, 2004.

[17]Jenkins, L. M., Khorrami, M. R., and Choudhari, M. M., "Characterization of Unsteady Flow Structures Near Leading-Edge Slat: Part I. PIV Measurements," AIAA Paper 2004-2801, 2004.

[18]Choudhari, M. M. and Khorrami, M. R., "Effect of Three-Dimensional Shear-Layer Structures on Slat Cove Unsteadiness," *AIAA Journal*, Vol. 45, No. 9, 2007, pp. 2174–2186.

[19]Rakhshani, B. and Filippone, A., "Three-Dimensional CFD Analysis of Slat Noise," AIAA Paper 2008-0015, 2008.

[20]Imamura, T., Enomoto, S., Yokokawa, Y., and Yamamoto, K., "Three-Dimensional Unsteady Flow Computations Around a Conventional Slat of High-Lift Devices," *AIAA Journal*, Vol. 46, No. 5, 2008, pp. 1045–1053.

[21]Klausmeyer, S. M. and Lin, J., "Comparative Results from a CFD Challenge Over a 2D Three-Element High-Lift Airfoil," NASA TM 112858, May 1997.

[22]Lockard, D. P. and Choudhari, M. M., "Noise Radiation from a Leading-Edge Slat," AIAA Paper 2009-3101, 2009.

[23]Imamura, T., Enomoto, S., Yokokawa, Y., and Yamamoto, K., "Simulation of the Broadband Noise from a Slat Using Zonal LES/RANS Hybrid Method," AIAA Paper 2007-0226, 2007.

[24]Dierke, J., Appel, C., Siebert, J., Bauer, M., Siefert, M., and Ewert, R., "3D Computation of Broadband Slat Noise from Swept and Unswept High-Lift Wing Sections," AIAA Paper 2011-2905, 2011.

[25]Bauer, M. and Ewert, R., "Slat Noise Prediction using Discontinuous Galerkin Method and Stochastic Turbulent Sound Source," AIAA Paper 2010-3832, 2010.

[26]Lockard, D. P. and Choudhari, M. M., "The Effect of Cross Flow on Slat Noise," AIAA Paper 2010-3835, 2010.

[27]Lockard, D. P. and Choudhari, M. M., "The Variation of Slat Noise with Mach and Reynolds Numbers," AIAA Paper 2011-2910, 2011.

[28]Choudhari, M. M., Lockard, D. P., Khorrami, M. R., and Mineck, R. E., "Slat Noise Simulations: Status and Challenges," Proceedings of Inter-Noise 2011, ed. Hiroyuki Imaizumi, Osaka, Japan, Sept. 4-7, 2011.

[29]Kaepernick, K., Koop, L., and Ehrenfried, K., "Investigation of the Unsteady Flow Field inside a Leading Edge Slat Cove," AIAA Paper 2005-2813, 2005.

[30]Andreou, C., Graham, W., and Shin, H. C., "Aeroacoustic Study of Airfoil Leading Edge High-Lift Devices," AIAA Paper 2006-2515, 2006.

[31]Imamura, T., Ura, H., Yokokawa, Y., Hirai, T., and Yamamoto, K., "Numerical and Experimental Research of Low-Noise Slat using Simplified High-lift Model," AIAA Paper 2008-2918, 2008.

[32]Rumsey, C. L., Biedron, R. T., and Thomas, J. L., "CFL3D: Its History and Some Recent Applications," NASA TM 112861, May 1997, presented at the Godonov's Method for Gas Dynamics Symposium, Ann Arbor, MI.

[33]Menter, F. R., "Two-equation Eddy-Viscosity Turbulence Models for Engineering Applications," *AIAA Journal*, Vol. 32, No. 8, 1994, pp. 1598–1605.

[34]Vatsa, V. N. and Lockard, D. P., "Assessment of Hybrid RANS/LES Turbulence Models for Aeroacoustics Applications," AIAA Paper 2010-4001, 2010.

[35]Chin, V. D., Peters, D. W., Spaid, F. W., and McGhee, R. J., "Flowfield Measurements about a Multi-element Airfoil at High Reynolds Numbers," AIAA Paper 1993-3137, 1993.

[36]Ffowcs Williams, J. E. and Hawkings, D. L., "Sound Generation by Turbulence and Surfaces in Arbitrary Motion," *Philosophical Transactions of the Royal Society*, Vol. A264, No. 1151, 1969, pp. 321–342.

[37]Lockard, D. P., "A Comparison of Ffowcs Williams-Hawkings Solvers for Airframe Noise Applications," AIAA Paper 2002-2580, 2002.

[38]Seo, J. H., Chang, K. W., and Moon, Y. J., "Aerodynamic Noise Prediction for Long-Span Bodies," AIAA Paper 2006-2573, 2006.

American Institute of Aeronautics and Astronautics